Journal of Chemistry and *Environment*

Elemental Mercury Removal from Natural Gas Using Nano-Tio₂

Mohamed A. Mandor[1], F. I. El-Hosiny[2], Y. M. Moustafa[1], Mohamed A. Ebiad[1], Mohamed Bakry Masod[1], Ahmed A. Salem[1], A. A. Elfadly[1]

[1]Analysis and Evaluation Department, Egyptian Petroleum Research Institute, Cairo, Egypt

[2]Chemistry Department, Faculty of science, Ain Shams University, Cairo, Egypt

Correspondence: badie2006@yahoo.com

Abstract

The study focused on the utilization of titanium dioxide (TiO_2) as a photo-catalyst for the treatment of natural gas contaminated with elemental mercury (Hg^0). The catalyst was carefully characterized using various physical techniques, including transmission electron microscopy (TEM), energy dispersive X-ray analysis (EDAX), UV-visible diffuse reflectance spectroscopy (DRS), Brunauer-Emmett-Teller (BET), X-ray photoelectron spectroscopy (XPS), and X-ray diffraction analysis (XRD). The results clearly demonstrated that TiO_2 exhibited outstanding efficacy in oxidizing Hg^0 when exposed to UV light. This phenomenon was ascribed to the excitation of photoelectrons within the valence band, leading to their transfer to the conduction band, generating photo-induced electrons that acted as reactive agents responsible for converting Hg^0 into HgO. Notably, the activity of TiO_2 under UV-visible light was significantly lower compared to TiO_2 under UV light. The overall findings indicated that TiO_2 under UV light exhibited the highest removal capacity, measured at 31.74 µg/g, followed by TiO_2 under UV-visible light at 25.91 µg/g, and TiO_2 in the dark at 20.89 µg/g. The study underscores the promising potential of TiO_2 photo-catalyst for effectively eliminating Hg^0 contamination in natural gas.

Keywords: Elemental mercury (Hg^0), Photo-catalysis, TiO_2, UV, UV-visible

1.   Introduction

Natural gas utilization as a vital fossil fuel in various human activities can lead to the presence of heavy metal contaminants, such as Hg and As, which present a substantial threat to both the environment and human health, which occur naturally [1, 2]. Among these contaminants, the highly volatile form of mercury (Hg^0) is of particular concern due to its volatility, neurotoxicity, tendency to bioaccumulate, and persistent nature. "The World Health Organization (WHO)" recognizes the significance of safeguarding organisms from the potential harm posed by it [3]. It has an unpleasant economic effect through natural gas processing plants [4, 5], even a small amount of mercury can cause significant damage to the heat exchangers with aluminum structure that are commonly utilized in cryogenic temperature processes used in LNG plants or naphtha crackers for olefin production [5, 6]. Also, mercury released to the environment through combustion of natural gas is constantly increasing from different sources in line with the Global Mercury Assessment of UNEP [7]. There are three types of mercury: elemental Hg^0, oxidized Hg^{2+}, and particulate Hg^p [8–11], Among these, elemental mercury (Hg^0) is the most common form found in natural gas [5, 12]. Numerous techniques have been researched for eliminating Hg^0, such as adsorption, conventional chemical oxidation, advanced oxidation, and catalytic oxidation, which

encompasses photocatalytic oxidation procedures [13-18]. Mercury's oxidized forms, commonly represented as Hg^{2+} species, have garnered significant attention due to their propensity to be efficiently captured by conventional control devices. This property leads to increased solubility in water and enhanced adsorption onto particles. Recognizing this characteristic, our study specifically targeted photocatalytic oxidation as a potential approach to address the issue.

TiO_2 is a widely favoured photocatalyst primarily due to its affordability, non-toxic nature, and advantageous band edge positions [19]. Its extensive use is attributed to its ability to harness the energy of light and convert it into chemical energy, thereby accelerating the reaction rate of various chemical processes [20]. Its exceptional properties render it an ideal choice for diverse applications, including water purification, air pollution control, and hydrogen production [36–38]. Additionally, its stability and durability under harsh conditions make it a reliable and efficient choice for industrial and environmental applications [19].

The majority of research in the field of photocatalytic removal of elemental mercury has primarily concentrated on flue gases. This preference stems from the fact that flue gases are more amenable to photocatalytic oxidation processes compared to natural gas. This is mainly due to the presence of components such as NOx, SO_2, H_2O, and HCl in flue gases, which facilitate the photooxidation process of Hg^0 [24, 25].

The study aims to investigate the effectiveness of TiO_2 as a photocatalyst for removing elemental mercury from natural gas under three different conditions: in the dark, in UV light, and in UV-visible light. The experiment will measure the removal efficiency of mercury using TiO_2 in each condition to determine which is the most effective. This information could be useful for optimizing the process of mercury removal in natural gas production. The study could also contribute to a better understanding of the mechanisms involved in photocatalytic reactions

using TiO_2, and provide insights into the factors that affect their performance.

2. Materials and Methods

2.1 Materials

TiO_2 nanoparticles were produced through the sol-gel technique using Titanium tetraisopropoxide as the starting material, HNO_3 bought from Merck and AR grade isopropanol procured from SD's Fine Chemicals (Pty) Ltd.

2.2 Synthesis of Catalyst

To prepare TiO_2 nanoparticles, a sol-gel method was used with 4 mL of Titanium tetraisopropoxide (TTIP) precursor in 10 mL of isopropanol. After undergoing agitation for 30 minutes at ambient temperature, the solution was subjected to forced hydrolysis through the addition of a solution containing isopropanol, deionized water, and HNO_3. The mixture stirred for two hours until a homogeneous and viscous solution was achieved. HNO_3 served as an acid catalyst to improve the hydrolysis and condensation rates [26]. Afterward, the solution was subsequently subjected to drying in an oven at 80°C for a duration of 2 hours, followed by a heat treatment process at 500°C for an additional 2 hours.

2.3 Characterization

The samples underwent characterization using various techniques, involving X-ray diffraction (Bruker XRD), transmission electron microscopy (JEOL 2100F TEM), and energy-dispersive X-ray spectroscopy (EDS), Surface area BET (NOVA2000) and UV/vis reflectance spectroscopy. The UV-visible diffuse reflectance spectra (DRS) were acquired using a Perkin Elmer Lambda 35 UV-visible spectrophotometer, which was equipped with an integrating sphere assembly. $BaSO_4$ was used as the reflectance standard for the measurements. K-ALPHA instrument for X-ray photoelectron spectroscopy (XPS) from (Thermo Fisher Scientific, USA) with monochromatic Al K-alpha radiation were used, which covered a range of 10 to 1350 eV. The spot size was 400 micrometers, and the pressure was maintained at 10-9 mbar. The full spectrum pass energy was set to 200 eV, and the

2.4 Photocatalytic activity test

The objective of the experiment was to assess the efficacy of TiO$_2$ catalyst in photo-catalytically removing elemental mercury. A quartz tube bed filled with glass beads and photocatalyst was used for the experiment. The weight ratio of catalyst to glass beads was 0.1:0.7g, with the glass beads performing as support for the catalyst and ensuring an even distribution of catalyst particles within the bed. The bed was exposed to two different UV wavelengths, i.e., 253.7 nm and 365 nm, as well as a dark medium. The mercury concentration before and after the bed was measured using a Nippon WA-4 instrument (an atomic absorption spectroscopy technique). The experiment involved the preparation of the catalysts by packing them with glass beads in the quartz tube bed. To determine the least effective temperature for catalyst activity, the performance of TiO$_2$ was assessed at three different media conditions: Dark, UV, and UV-visible. The activity of elemental mercury removal was evaluated using the initial and final concentration of mercury passing through the catalyst bed using equation 1.

$$q = \frac{Q \int_0^t (C_{in} - C_{out})\, dt}{m} \quad (1)$$

The formula provided is used to calculate the dynamic Hg^0 adsorption capacity, where q is in units of µg·g^{-1}. Q represents the total gas flow rate, measured in m^3·min^{-1}; t represents the time elapsed, measured in minutes; m represents the mass of sorbent used, measured in grams; C$_{in}$ represents the real-time concentration of Hg^0 at the inlet, measured in µg·m^{-3}; and C$_{out}$ represents the real-time concentration of Hg^0 at the outlet, also measured in µg·m^{-3}.

3. Results and discussion

The results obtained from the physico-chemical characterization techniques are now being discussed.

3.1 X-ray diffraction analysis

X-ray diffraction (XRD) is a valuable technique for analyzing the crystal structure and average size of nanoparticles. It provides insights into the atomic arrangement within a sample and captures the diffraction pattern resulting from the interaction of X-rays with the sample. The pattern of TiO$_2$ nanoparticles (XRD) was analyzed to determine its crystal structure.
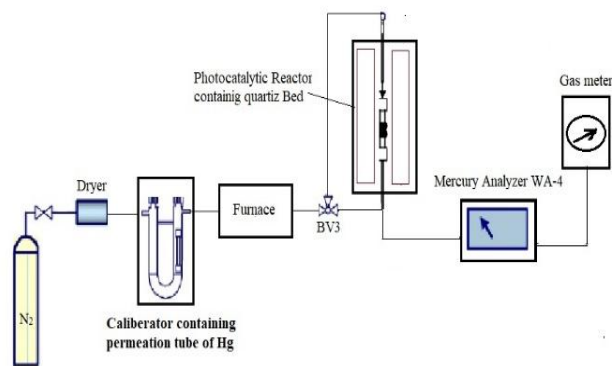

Figure1: Photocatalytic system diagram for Elemental mercury removal.

The results showed that the nanoparticles have the crystalline features of anatase, as indicated by the peaks in the pattern matching to the anatase phase at specific 2θ values 25.43º, 38º, 48.01º, 54.08º, 55.36º, and 62.78º. The observed peaks in the X-ray diffraction pattern are identified by their corresponding hkl values enclosed in parentheses, such as (1 0 1), (1 1 2), (2 0 0), (1 0 5), (2 1 1), and (2 0 4). The main diffraction peak in the anatase XRD pattern is at 2θ = 25.43°, matches with the (1 0 1) plane. The size of the nanoparticles was determined by calculating the full width at half maximum (FWHM) of the (1 0 1) diffraction peak and applying Scherrer's equation (number 2). The equation establishes a correlation between the average crystallite size (D), the wavelength of the X-ray source (λ), the FWHM of the diffraction peak (β), and the diffraction angle (θ). The result provides an average size estimate for the nanoparticles, but does not account for the size distribution or shape.

D = Kλ/β cosθ (2)

In the equation, D represents the crystal size of the sample,

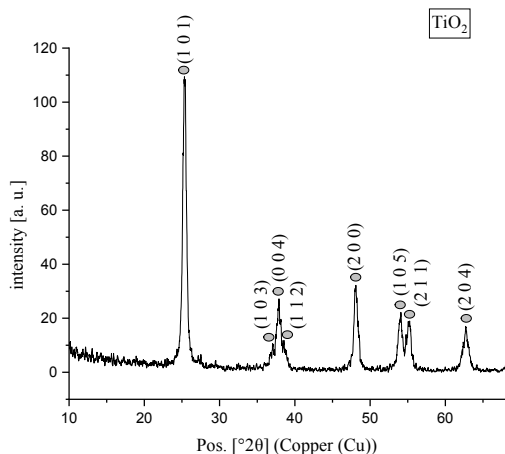**Figure 2:** XRD patterns of undoped TiO_2 catalyst λ denotes the wavelength of the X-ray (1.54056 Å), β corresponds to the full width at half maximum (FWHM) of the diffraction peak in radians, K is a coefficient (0.89), and θ represents the diffraction angle at the peak maximum. The crystal size of TiO_2 is found to be 20.31 nm.

3.2 HR-TEM characterization and EDAX spectrum

The TEM image shown in figure 3a reveals the shape, structure, and range of sizes of the synthesized TiO_2 nanoparticles. The irregular spherical shape observed suggests that the nanoparticles are not perfectly round, but instead have variations in shape, likely due to the synthesis method used. The small particle size observed between 15 to 35 nm indicates that the nanoparticles are relatively small, which is important for achieving high surface area and reactivity in photocatalysis. The uniform size distribution observed suggests that the synthesis method used is efficient and reproducible.

The EDAX spectrum shown in figure 3b provides elemental information about the sample, indicating the presence of titanium and oxygen, which is expected for TiO_2. This further confirms the successful synthesis of TiO_2 nanoparticles. Overall, the combination of TEM and EDAX analysis provides important evidence about the morphology and size distribution of the synthesized TiO_2 nanoparticles.

3.3 UV–visible diffuse reflectance spectra (DRS)

The (UV-vis DRS) was used to examine the optical properties of the samples. Results, shown in Figure 4a, indicate that TiO_2 exhibits a pronounced absorption band in the ultraviolet (UV) region, ranging from 200 to 380 nm. However, there is little absorption in the visible light region (above 400 nm). This is mainly due to electrons transmission from valence to conduction band of TiO_2. Nevertheless, it is evident that the TiO2 samples exhibit a significant absence of absorption in the visible light region, which extends beyond 400 nm [27].
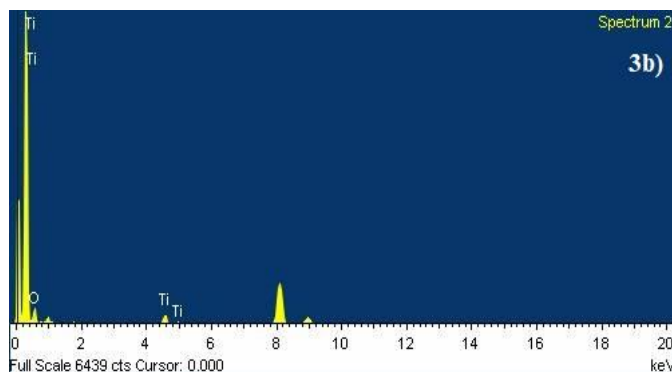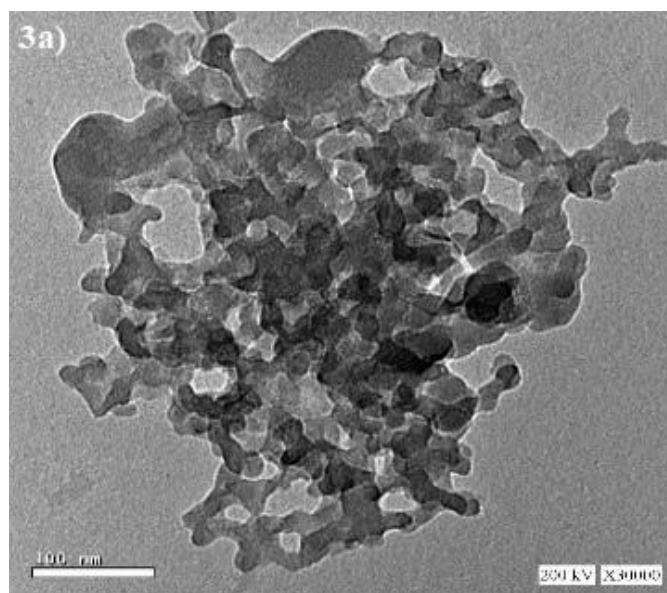

Figure 3: Images of a) TEM and b) EDAX Spectra of TiO_2.

To estimate the band gap energy (Eg) of the samples, the Kubelka-Munk equation (3) was used to determine band gap energy (Eg) and the equation assumes an infinitely thick sample, disregarding the effects of sample thickness and holder on reflectance (R) [28].

$$\frac{\kappa}{s} = \frac{(1 - R_\infty)^2}{2R_\infty} = F(R_\infty)$$

(3)

101

where BaSO$_4$ was used as the reference material for white light. The equation involves two coefficients, K and S, and the remission or K-M function, F(R$_\infty$), where R$_\infty$ is the final reflectance, obtained by dividing the sample reflectance by the reference reflectance. The wavelength was exchanged to electron volts (eV) by dividing 1240 by the wavelength. R$_\infty$ is the square root of the product of energy and R. (Eg) was obtained from the slope of the F vs R$_\infty$ plot of the prepared TiO$_2$ as shown in Figure 4b was determined to be 3.3 eV [28].
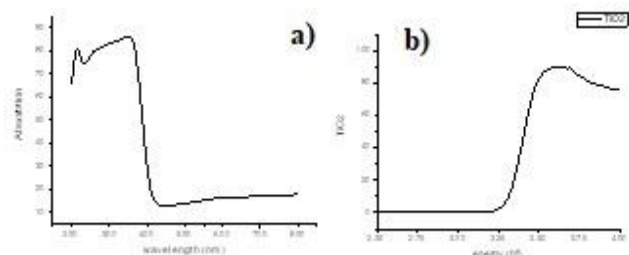

Figure 4: a) UV–Vis-DRS and b) the band gap energy of TiO$_2$.

3.4 BET Characterization

A Type IV isotherm is typically observed in mesoporous materials and is commonly associated with materials that possess slit-shaped or cylindrical pores. The hysteresis loop indicates the presence of mesopores, which are formed when the particles that make up the material agglomerate during synthesis. The particles form voids or spaces between them, which are the meso-pores. The shape of the hysteresis loop gives information regarding the size and shape of the meso-pores. In the case of H3 loop, it suggests the observed hysteresis loop suggests the existence of slit-shaped pores and/or panel-shaped particles, which means that the pores have a long and narrow shape.

The surface area of TiO$_2$, determined using the BET method, is 43.034 m^2/g, which indicates that TiO$_2$ has a relatively low surface area. However, the presence of meso-pores in the material suggests that it may have good accessibility for reactants and products, which is beneficial for catalytic applications. The pore size distribution analysis revealed that TiO$_2$ exhibits a range of pore sizes

from 4 to 9 nm, an average pore diameter (3.650 nm) and a pore volume (0.098 cc/g). These findings confirm the mesoporous nature of the surface pores in TiO$_2$ [29, 30]
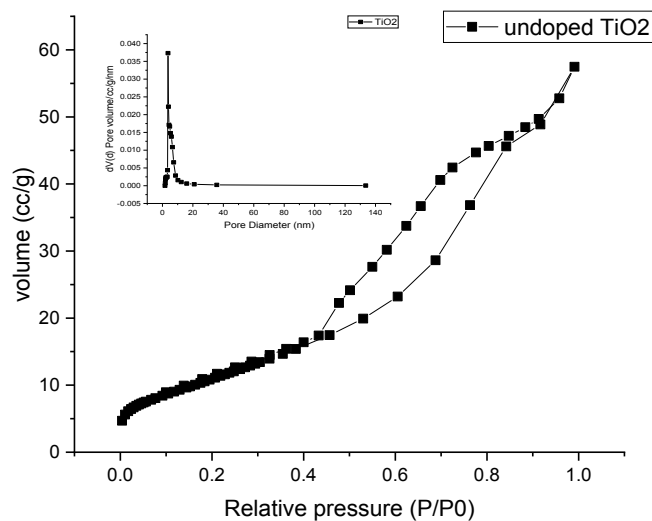

Figure 5: N$_2$-adsorption–desorption isotherm and Pore Size distributions of TiO$_2$.

As shown in figure 5. Where, in this type of adsorption isotherm, as the relative pressure increases, both the adsorption volume and the adsorption rate show a corresponding increase. Overall, the presence of a Type IV isotherm and the analysis of pore size distribution suggest that the TiO$_2$ material exhibits a mesoporous structure characterized by slit-shaped or cylindrical pores. Although it has a relatively low surface area, it offers favourable accessibility for reactants and products. These properties indicate its potential usefulness in catalytic applications.

3.5 XPS

XPS is commonly used, as shown in Figure 6, to investigate the chemical bonding and electronic structure of metal oxides, including TiO$_2$. Specifically, the Ti2p and O1s spectra were examined to gain insights into the bonding characteristics. Based on the provided data, 458.64 eV and 464.34 eV are the binding energies of Ti2P peaks that are recognized to titanium oxide lattice, corresponding to the binding energy of highest oxidation state of Ti atoms in TiO$_2$ nanoparticles (Ti^{4+} ions). TiO$_2$ nanoparticles did not reveal any peaks associated with reduced titanium Ti^{3+}, indicating
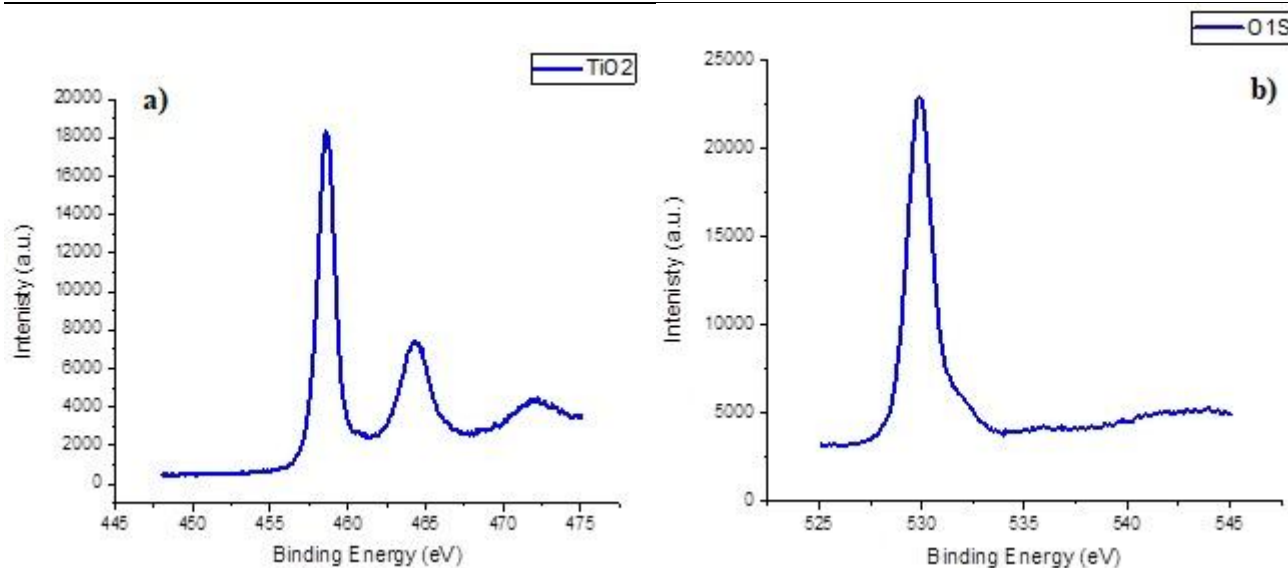
Figure 6: XPS spectral of TiO_2 a) Ti2p and b) O1s spectra.

Overall, the XPS analysis suggests that the studied TiO_2 nanoparticles are of high purity and possess a well-defined crystalline structure. These characteristics make them suitable for potential applications in various fields, including photocatalysis, energy storage, and biomedical engineering.
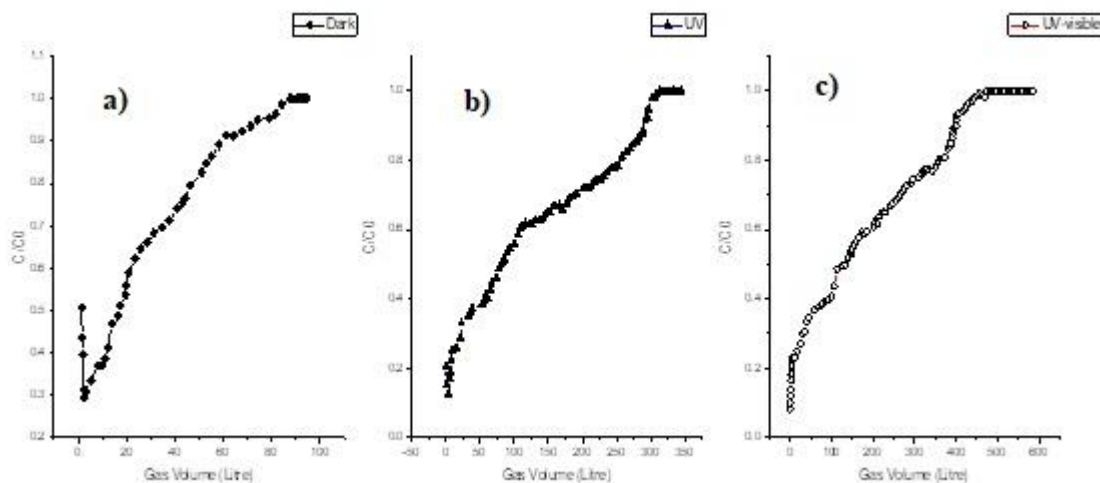

Figure 7: Break through curves of Hg^0 photo-oxidation and adsorption over TiO_2 in a) Dark, b) UV light and c) UV-visible light.
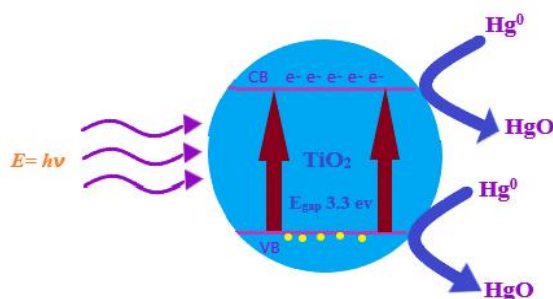

Figure 8: Impact of light source on the mercury removal efficiency of TiO_2.

103

the absence of defects in the material [31]. The O1s spectrum reveals two distinct peaks. The peak observed at a lower binding energy of approximately 530 eV is associated with lattice oxygen atoms (O^{2-}), indicating their presence within the TiO_2 structure. On the other hand, the peak observed at a higher binding energy of approximately 532 eV can be attributed to surface hydroxyl groups (OH^-) or adsorbed water molecules. This information provides insights into the chemical environment and surface properties of the TiO_2 nanoparticles, highlighting the presence of both oxygen species within the material [32].

3.6 Photo-Catalytic Activity

The experimental setup for evaluating the photocatalytic activity of TiO_2 involved the passage of a gas stream containing elemental mercury through a quartz tube filled with the catalyst material. The concentration of elemental mercury was then measured after it passed through the catalyst. The experiments were conducted under various conditions, including darkness, UV light, and UV-visible light. The removal capacity of TiO_2 was found to be 20.894

$\mu g. g^{-1}$ in 12 hours in the dark shown in figure 7a, 25.913 $\mu g. g^{-1}$ in 20 hours under UV-visible light shown in figure 7c, and 31.746 $\mu g. g^{-1}$ in 27 hours under UV light displayed in figure 7b.

As shown in Figure 7b, the higher removal capacity under UV light can be explained by the movement of photoelectrons from the valence band to the conduction band of TiO_2, producing photo-generated electrons and holes [33]. This process generates highly reactive species, for example hydroxyl radicals, that have the ability to oxidize Hg^0 to Hg^{2+}. The Hg^{2+} ions that are formed can readily adsorb onto the surface of the TiO_2 particles, effectively removing them from the gas stream as shown in figure 8.

Changing from a UV lamp (253.7 nm) to a UV-visible lamp (365 nm) alters the emitted light wavelength and energy. The lower energy of the UV-visible lamp leads to a reduced capacity for Hg^0 removal compared to the UV lamp. This is attributed to insufficient generation of electrons and holes for efficient Hg^0 photo-oxidation [34].

Table 1 The Brunauer–Emmett–Teller (BET) surface area result.

Sample	Pore volume ($cm^3.g^{-1}$)	Average pore size (nm)	SBET ($m^2. g^{-1}$)
TiO$_2$	0.098	3.650	43.034

Table 2: Capacity of Hg^0 removal over TiO_2 in µg/g.

Radiation	Q (Adsorption)
Dark	20.89
UV	31.74
UV-visible	25.91

4. CONCLUSION

The study aimed to investigate the photo-catalytic activity of TiO2 in the removal of elemental mercury from a gas stream under various light conditions. The results showed

that TiO_2 exhibited higher removal capacity under UV light 31.74 µg/g compared to UV-visible 25.91 µg/g and dark 20.89 µg/g conditions, owing to the presence of highly reactive species produced during the photocatalytic process

leads to the oxidation of elemental mercury (Hg^0) to Hg^{2+}. This highlights the potential of photocatalysts such as TiO_2 as an eco-friendly and economical solution for effectively removing elemental mercury from natural gas. However, further research is needed to optimize the photo-catalytic performance of TiO_2 and to develop effective methods for scaling up the process of industrial applications. Also, the efficiency of the photo-catalytic reaction is significantly influenced by the energy emitted by the light source employed in the process. Hence, selecting a light source that can generate an adequate amount of photo-generated electrons and holes is essential for ensuring efficient photo-catalytic reactions.

Authors Contribution

M.A.E., A.A.E and M.B.M have the main idea of the manuscript. M.A.M and A.A.S wrote the the manuscript. Y.M.M. and F.I.E. revised the manuscript and provide suggestions.

Conflicts of Interest

There are no conflicts of interest reported by the writers.

Acknowledgment

Data Availability statement

The data presented in this study are available on request from the corresponding author.

REFERENCES

1. R. Khunphonoi, P. Khamdahsag, S. Chiarakorn, N. Grisdanurak, A. Paerungruang, and S. Predapitakkun, "Enhancement of elemental mercury adsorption by silver supported material," J. Environ. Sci. (China), vol. 32, pp. 207–216, 2015, doi: 10.1016/j.jes.2015.01.008.

2. K. J. Irgolic and B. K. Puri, "Organic Arsenic Compounds in Petroleum and Natural Gas," in Metal Speciation in the Environment, Berlin, Heidelberg: Springer Berlin Heidelberg, 1990, pp. 377–389. doi: 10.1007/978-3-642-74206-4_20.

3. World Health Organization (WHO), "Elemental mercury and inorganic mercury compounds: human health aspects," 2003. [Online]. Available: http://www.who.int/ipcs/publications/cicad/en/cicad50.pdf?ua=1

4. M. D. Bingham, "Field Detection and Implications of Mercury in Natural Gas," SPE Prod. Eng., vol. 5, no. 02, pp. 120–124, May 1990, doi: 10.2118/19357-PA.

5. A. A. El-Feky, W. El-Azab, M. A. Ebiad, M. B. Masod, and S. Faramawy, "Monitoring of elemental mercury in ambient air around an Egyptian natural gas processing plant," J. Nat. Gas Sci. Eng., vol. 54, no. January, pp. 189–201, Jun. 2018, doi: 10.1016/j.jngse.2018.01.019.

6. M. F. Ezzeldin, Z. Gajdosechova, M. B. Masod, T. Zaki, J. Feldmann, and E. M. Krupp, "Mercury Speciation and Distribution in an Egyptian Natural Gas Processing Plant," Energy & Fuels, vol. 30, no. 12, pp. 10236–10243, Dec. 2016, doi: 10.1021/acs.energyfuels.6b02035.

7. UNEP, "Global Mercury Assessment," 2018. [Online]. Available: https://www.amap.no/documents/doc/global-mercury-assessment-2018/1757

8. S. Zhao, D. Pudasainee, Y. Duan, R. Gupta, M. Liu, and J. Lu, "A review on mercury in coal combustion process: Content and occurrence forms in coal, transformation, sampling methods, emission and control technologies," Progress in Energy and Combustion Science, vol. 73. Pergamon, pp. 26–64, Jul. 01, 2019. doi: 10.1016/j.pecs.2019.02.001.

9. D. STREETS et al., "Anthropogenic mercury emissions in China," Atmos. Environ., vol. 39, no. 40,

pp. 7789–7806, Dec. 2005, doi: 10.1016/j.atmosenv.2005.08.029.

10. Y. Wang et al., "Experimental study on mercury transformation and removal in coal-fired boiler flue gases," Fuel Process. Technol., vol. 90, no. 5, pp. 643–651, May 2009, doi: 10.1016/j.fuproc.2008.10.013.

11. G. Kos et al., "Evaluation of discrepancy between measured and modelled oxidized mercury species," Atmos. Chem. Phys., vol. 13, no. 9, pp. 4839–4863, May 2013, doi: 10.5194/acp-13-4839-2013.

12. M. A. Ebiad, M. Bakry, and N. City, "Adsorption of Hg 2 + using modified sulfur-impregnated activated carbon from olive stone," Mansoura J. Chem., vol. 42, no. 2, p. 16, 2016.

13. P. Wang et al., "Catalytic oxidation of Hg0 by MnOx-CeO$_2$/γ-Al$_2$O$_3$ catalyst at low temperatures," Chemosphere, vol. 101, pp. 49–54, 2014, doi: 10.1016/j.chemosphere.2013.11.034.

14. J. Y. Lee, Y. Ju, T. C. Keener, and R. S. Varma, "Development of cost-effective noncarbon sorbents for Hg^0 removal from coal-fired power plants," Environ. Sci. Technol., 2006, doi: 10.1021/es051951l.

15. Z. Tan et al., "Gas-phase elemental mercury removal by novel carbon-based sorbents," Carbon N. Y., vol. 50, no. 2, pp. 362–371, 2012, doi: 10.1016/j.carbon.2011.08.036.

16. N. Saman et al., "Enhanced elemental mercury removal by facile sulfurization of agrowaste chars," Chem. Eng. Res. Des., vol. 144, pp. 198–208, 2019, doi: 10.1016/j.cherd.2019.02.010.

17. Z. Liu, W. Yang, W. Xu, and Y. Liu, "Removal of elemental mercury by bio-chars derived from seaweed impregnated with potassium iodine," Chem.

Eng. J., vol. 339, no. February, pp. 468–478, 2018, doi: 10.1016/j.cej.2018.01.148.

18. W. Ji, Z. Shen, M. Fan, P. Su, Q. Tang, and C. Zou, "Adsorption mechanism of elemental mercury (Hg^0) on the surface of MnCl$_2$ (1 1 0) studied by Density Functional Theory," Chem. Eng. J., vol. 283, pp. 58–64, 2016, doi: 10.1016/j.cej.2015.06.033.

19. E. Pitoniak, C. Y. Wu, D. W. Mazyck, K. W. Powers, and W. Sigmund, "Adsorption enhancement mechanisms of silica-titania nanocomposites for elemental mercury vapor removal," Environ. Sci. Technol., 2005, doi: 10.1021/es049202b.

20. J. An et al., "Performance evaluation of non-thermal plasma injection for elemental mercury oxidation in a simulated flue gas," J. Hazard. Mater., vol. 268, pp. 237–245, 2014, doi: 10.1016/j.jhazmat.2014.01.022.

21. P. Fang, C. P. Cen, X. M. Wang, Z. J. Tang, Z. X. Tang, and D. S. Chen, "Simultaneous removal of SO$_2$, NO and Hg^0 by wet scrubbing using urea + KMnO4 solution," Fuel Process. Technol., vol. 106, 2013, doi: 10.1016/j.fuproc.2012.09.060.

22. F. Ding, Y. Zhao, L. Mi, H. Li, Y. Li, and J. Zhang, "Removal of gas-phase elemental mercury in flue gas by inorganic chemically promoted natural mineral sorbents," Ind. Eng. Chem. Res., vol. 51, no. 7, pp. 3039–3047, 2012, doi: 10.1021/ie202231r.

23. Y. Zhao, F. Xue, X. Zhao, T. Guo, and X. Li, "Experimental study on elemental mercury removal by diperiodatonickelate (IV) solution," J. Hazard. Mater., vol. 260, pp. 383–388, 2013, doi: 10.1016/j.jhazmat.2013.05.040.

24. Z. Barnea, T. Sachs, M. Chidambaram, and Y. Sasson, "A novel oxidative method for the absorption of Hg^0 from flue gas of coal fired power plants using task specific ionic liquid scrubber," J. Hazard. Mater., vol.

244–245, pp. 495–500, 2013, doi: 10.1016/j.jhazmat.2012.10.067.

25. T. Abbas et al., "Mercury capture from natural gas by carbon supported ionic liquids: Synthesis, evaluation and molecular mechanism," Fuel, vol. 177, pp. 296–303, Aug. 2016, doi: 10.1016/j.fuel.2016.03.032.

26. G. Cheng, Q. Zhang, and B. Bai, "Removal of Hg0 from flue gas using Fe-based ionic liquid," Chem. Eng. J., vol. 252, pp. 159–165, 2014, doi: 10.1016/j.cej.2014.05.007.

27. B. Shen et al., "Simultaneous removal of NO and Hg0using Fe and Co co-doped Mn-Ce/TiO$_2$ catalysts," Fuel, 2018, doi: 10.1016/j.fuel.2018.03.080.

28. Y. Cao et al., "Impacts of halogen additions on mercury oxidation, in a slipstream Selective Catalyst Reduction (SCR), reactor when burning sub-bituminous coal," Environ. Sci. Technol., vol. 42, no. 1, 2008, doi: 10.1021/es071281e.

29. Y. Gao et al., "A Critical Review on the Heterogeneous Catalytic Oxidation of Elemental Mercury in Flue Gases," Environ. Sci. Technol., vol. 47, no. 19, pp. 10813–10823, Oct. 2013, doi: 10.1021/es402495h.

30. Y. Xu, Q. Zhong, and X. Liu, "Elemental mercury oxidation and adsorption on magnesite powder modified by Mn at low temperature," J. Hazard. Mater., vol. 283, pp. 252–259, 2015, doi: 10.1016/j.jhazmat.2014.09.034.

31. H. Wang, S. Zhou, L. Xiao, Y. Wang, Y. Liu, and Z. Wu, "Titania nanotubes-A unique photocatalyst and adsorbent for elemental mercury removal," Catal. Today, vol. 175, no. 1, pp. 202–208, 2011, doi: 10.1016/j.cattod.2011.03.006.

32. Y. Yuan et al., "Electrospun metal oxide–TiO$_2$ nanofibers for elemental mercury removal from flue gas," J. Hazard. Mater., vol. 227–228, pp. 427–435, 2012, doi: 10.1016/j.jhazmat.2012.05.003.

33. J. Yang, S. Ma, Y. Zhao, H. Li, J. Zhang, and C. Zheng, "Elemental Mercury Removal from Flue Gas over TiO$_2$ Catalyst in an Internal-Illuminated Honeycomb Photoreactor," Ind. Eng. Chem. Res., vol. 57, no. 51, pp. 17348–17355, 2018, doi: 10.1021/acs.iecr.8b04417.

34. S. M. Gupta and M. Tripathi, "A review of TiO$_2$ nanoparticles," Chinese Sci. Bull., vol. 56, no. 16, pp. 1639–1657, 2011, doi: 10.1007/s11434-011-4476-1.

35. A. L. Linsebigler, G. Lu, and J. T. Yates, "Photocatalysis on TiO2 Surfaces: Principles, Mechanisms, and Selected Results," Chem. Rev., vol. 95, no. 3, pp. 735–758, 1995, doi: 10.1021/cr00035a013.

36. Y. Wen et al., "Spectrophotometric determination of arsenic in environmental and biological samples," INDIAN J. CHEM. TECHNOL, vol. 5, no. 1, pp. 1–7, Dec. 2014, doi: 10.1016/j.molcata.2012.07.020.

37. M. R. Pai et al., "A comprehensive study on sunlight driven photocatalytic hydrogen generation using low cost nanocrystalline Cu-Ti oxides," Sol. Energy Mater. Sol. Cells, vol. 154, pp. 104–120, 2016, doi: 10.1016/j.solmat.2016.04.036.

38. P. Supphasrirongjaroen, P. Praserthdam, J. Panpranot, D. Na-Ranong, and O. Mekasuwandumrong, "Effect of quenching medium on photocatalytic activity of nano-TiO$_2$ prepared by solvothermal method," Chem. Eng. J., vol. 138, no. 1–3, pp. 622–627, 2008, doi: 10.1016/j.cej.2007.09.035.

39. H. Li, C. Y. Wu, Y. Li, L. Li, Y. Zhao, and J. Zhang, "Role of flue gas components in mercury oxidation over TiO2 supported MnOx-CeO$_2$ mixed-oxide at low

temperature," J. Hazard. Mater., vol. 243, pp. 117–123, 2012, doi: 10.1016/j.jhazmat.2012.10.007.

40. S. Zhao, D. Pudasainee, Y. Duan, R. Gupta, M. Liu, and J. Lu, "A review on mercury in coal combustion process: Content and occurrence forms in coal, transformation, sampling methods, emission and control technologies," Progress in Energy and Combustion Science, vol. 73. Pergamon, pp. 26–64, Jul. 2019. doi: 10.1016/j.pecs.2019.02.001.

41. S. Ananth, T. Arumanayagam, P. Vivek, and P. Murugakoothan, "Direct synthesis of natural dye mixed titanium dioxide nano particles by sol–gel method for dye sensitized solar cell applications," Optik (Stuttg)., vol. 125, no. 1, pp. 495–498, Jan. 2014, doi: 10.1016/j.ijleo.2013.07.018.

42. N. Sobana, M. Muruganadham, and M. Swaminathan, "Nano-Ag Particles Doped TiO_2 for Efficient Photodegradation of Direct Azo Dyes Nano-Ag particles doped TiO_2 for efficient," J. Mol. Catal. A Chem., vol. 258, no. November 2016, pp. 124–132, 2006, doi: 10.1016/j.molcata.2006.05.013.

43. J. G. Wen, "X-ray diffraction and reflectivity," in Practical Materials Characterization, New York, NY: Springer New York, 2014, pp. 189–229. doi: 10.1007/978-1-4614-9281-8_5.

44. W. Wang, P. Liu, M. Zhang, J. Hu, and F. Xing, "The Pore Structure of Phosphoaluminate Cement," Open J. Compos. Mater., vol. 02, no. 03, pp. 104–112, 2012, doi: 10.4236/ojcm.2012.23012.

45. M. Thommes et al., "Physisorption of gases, with special reference to the evaluation of surface area and pore size distribution (IUPAC Technical Report)," Pure Appl. Chem., vol. 87, no. 9–10, 2015, doi: 10.1515/pac-2014-1117.

46. D. Briggs, "Handbook of X Ray Photoelectron Spectroscopy: A Reference Book of Standard Spectra for Identification and Interpretation of XPS Data," in Handbook of Adhesion, Chichester, UK: John Wiley & Sons, Ltd, 2005, pp. 621–622. doi: 10.1002/0470014229.ch22.

47. K. Ubolchollakhat, L. Sikong, and W. Sangchay, "Effect of Ni-doped on surface of titaniumdioxide thin film," Dig. J. Nanomater. Biostructures, vol. 10, no. 4, pp. 1469–1473, 2015.

48. T. N. Obee, "Photooxidation of sub-parts-per-million toluene and formaldehyde levels on titania using a glass-plate reactor," Environ. Sci. Technol., vol. 30, no. 12, pp. 3578–3584, 1996, doi: 10.1021/es9602713.Society, 89(11), pp.2669-2676.

How to cite this article:

Mandor MA, El-Hosiny FI, Moustafa YM, Ebiad MA, Masod MB, Salem AA. (2023). Elemental Mercury Removal from Natural Gas Using Nano-Tio2. Journal of Chemistry and Environment. 2(1).p.98-108